Multiphase simulations and experiments of subaqueous granular collapse on an inclined plane in densely packed conditions: Effects of particle size and initial concentration

Cheng-Hsien Lee [*] and Jia-You Chen
Department of Marine Environment and Engineering, National Sun Yat-sen University, Kaohsiung 80424, Taiwan

(Received 1 September 2021; accepted 17 March 2022; published 7 April 2022)

Subaqueous granular collapse on an inclined plane was investigated by considering the effects of particle size and initial concentration in densely packed conditions. This study adopted the multiphase model developed by Lee [J. Fluid Mech. **907**, A31 (2021)], which can capture pore pressure feedback (an important mechanism in subaqueous granular flows). A new set of laboratory experiments were performed to validate the multiphase model with four different particle sizes (from fine sand to very coarse sand). Generally, the multiphase model can reproduce all the experimental collapse processes well. Four particle sizes and four initial concentrations were examined numerically. The simulated results reveal that both the volume of the sliding mass in the early stages (initial sliding volume) and the front speed increase with increasing particle size. In addition, increasing the initial concentration reduces the initial sliding volume and front speed. The simulated results suggest that the front speed can be expressed as a function of the initial sliding volume. A simplified force balance analysis was performed to examine why the particle size and the initial concentration affect the initial sliding volume.

DOI: 10.1103/PhysRevFluids.7.044301

I. INTRODUCTION

Subaqueous landslides can occur at the edge of continental shelves, submarine canyons, and bays [1]. When a landslide releases high amount of sediment, large waves (tsunamis) can be generated with the potential to threaten human life in the affected areas [2–4]. Additionally, the released sediment flows due to gravity and the resultant sedimentary density flow can break subaqueous pipelines [5] and cables [6]. Understanding the characteristics of subaqueous landslides and modeling them are crucial issues in the assessment of both tsunami hazards and geohazards for offshore installations.

Mechanically, a subaqueous landslide occurs when the driving stress exceeds the strength of the slope-forming material [1]. The flow and deposition processes are complicated two-phase phenomena in nature, involving granular dynamics, fluid dynamics, and fluid-particle interaction. To examine the physics behind subaqueous landslides, previous experimental studies examined a two-dimensional granular collapse in a fluid as an idealized model [7–12]. The findings are outlined below. Compared to subaerial granular collapse, subaqueous granular collapse has a slower spreading velocity owing to the increased drag force [7]. The initial packing (or the initial concentration) [8,9] is an important parameter that determines the contraction or dilation behavior in the early stage of collapse and further affects the pore pressure formation [8]. When the initial

[*]kethenlee@gmail.com

concentration is higher or lower than the critical concentration, the pore pressure, respectively, increases or decreases in the early stage of collapse, and the mobility of granular material also increases or decreases [8]. The particle size determines the permeability [13] and plays a role in changing the pore pressure. Finer particles (lower permeability) cause significant changes in the pore pressure, affecting the mobility [11,12]. The Stokes number (the ratio of particle inertia and fluid viscous effects) determines the rheological characteristics and friction in the flow process [10].

Regarding the modeling of subaqueous landslides, several depth-integrated models have incorporated the effects of initial packing and pore-pressure feedback [14–16]. The angle of dilation [17] was used in all models to characterize the shear-induced volume change. The Darcy law was used to compute the changes in pore pressure, and the sediment strength was determined by the Coulomb friction law. Bouchut *et al.* [18] successfully applied the depth-integrated model to reproduce the experiment of the subaqueous granular collapses [8]. Some depth-resolving models have also been developed based on the Eulerian-Eulerian framework [19–22], treating fluids and solids (particles) as two interpenetrating continuum media. Most of these models applied elastic relationships to compute the static solid pressure, which cannot reflect the shear-induced volume change accurately [20]. Shi *et al.* [23] modified the elastic relationships by incorporating the effect of shear on changing the static solid pressure. In contrast, Lee [24] proposed an evolution equation for the static solid pressure, in which shear and compression were considered. The evolution equation allowed the multiphase model to reflect the shear-induced volume change and pore-pressure feedback [24]. Lee [24] and Shi *et al.* [23] successfully used their model to reproduce the experiment of subaqueous granular collapses [8]. However, only one particle size was used in the experiment by Rondon *et al.* [8].

This study has two objectives. The first is to examine the ability of the model proposed by Lee [24] for simulating subaqueous landslides with different particle sizes. New laboratory experiments were conducted using four different particle sizes (from fine sand to very coarse sand) in densely packed conditions where the initial concentration exceeded the critical concentration. The experimental results were used to validate the model proposed by Lee [24].

The second objective is to numerically investigate the effect of particle size and initial concentration on the sliding body in the early stage of collapse (referred to as the initial sliding mass hereafter) and on the front speed. To the authors' knowledge, no studies have been devoted to these topics. The sliding volume is an important parameter for determining the tsunami wave height [25]. During the collapse process, the sliding volume varied temporally. Only in the early stage, the energy of the sliding material can be transferred to the main tsunami wave owing to the high propagation speed of the tsunami wave. The front speed is key to determining the hydrodynamic forces applied to a subaqueous facility from the sedimentary flow [26]. Bougouin and Lacaze [10] studied the speed of the sliding front for particle with diameter of 3 mm in a flat bed. In this study, four smaller particles were used.

II. EXPERIMENT, NUMERICAL MODEL, AND TEST CONDITIONS

This section first describes the experimental setup, and then introduces the model of Lee [24]. This is followed by a description of the numerical setup. Finally, the test conditions are summarized.

A. Experimental setup

The experimental setup is shown schematically in Fig. 1. The experiment used a 2-m long, 0.15-m wide, and 0.60-m high Perspex water tank equipped with a removable slope and a removable bed. Compared to a flat bed [7–11], using a slope allows the sedimentary flow more time to develop. The bottom and the slope were made of Perspex plates coated with very coarse sand of diameter $d = 1.29$ mm in an attempt to create a no-slip boundary condition [27]. A sand reservoir was created on the slope by a vertical gate with two lateral ends secured by two slots on the sidewalls. The bottom of the sand reservoir was located 0.15 m above the bed. The granular mass had a height of $H_i = 0.1$ m and a width of $L_i = 0.1$ m.

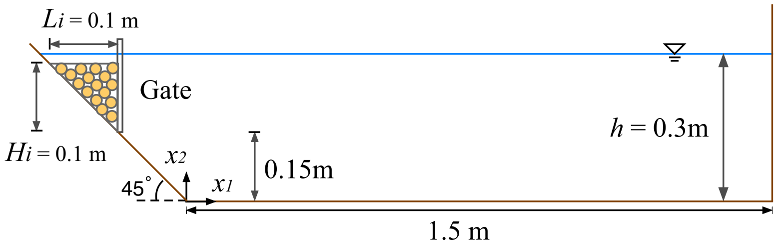

FIG. 1. Schematic of experimental setup.

Four particle sizes were studied: fine sand ($d = 0.2$ mm), medium sand ($d = 0.49$ mm), coarse sand ($d = 0.66$ mm), and very coarse sand ($d = 1.29$ mm). The density of each particle was ρ_s $=2580\,\mathrm{kg}/m^3 \pm 1\%$, the angle of repose was $\theta_r \approx 35^\circ$, and the random loose packing was $c_o = 0.54 \pm 1\%$, which was obtained by carefully spreading sands using a spoon into a two-liter beaker partially filled with water. $c_o = 0.54$ was close to the concentration of random loose packing for frictional spheres [28]. Tap water was used in the experiment; its density was $\rho_f = 1000\,\mathrm{kg}/m^3$ and its kinematic viscosity was $\nu_f = 10^{-6}$ m^2/s. The values of Stokes number (St $= [\rho_s(\rho_s/\rho_f - 1)gd^3]^{1/2}/\rho_f\nu_f$ with g being the acceleration of gravity) were 0.7, 2.7, 4.2, and 11.5 for the fine sand, the medium sand, the coarse sand, and the very coarse sand. The density ratio $(r = \rho_s/\rho_f)^{1/2}$ was 1.6.

The particles were poured into the reservoir. A whisk driven by a drill motor was used to suspend the particles. After all the particles were deposited, the resultant concentration c was $0.55 \pm 1\%$ for all the four types of sands [29]. The concentration of 0.55 was close to c_o. To generate a more dense granular material, a vibrating stick was inserted into the deposition every 0.04 m to consolidate the deposition, resulting in $c = 0.6 \pm 1.2\%$. The initial concentration of $c_i = 0.6$ was used in the experiment.

The two light panels were installed behind the tank. Shadow from the landslide mass was recorded by a sports camera (GoPro Hero 8). The particles were indistinguishable in the video-recorded images, preventing from using a particle image velocimeter to obtain the particle velocity. The frame rate was fixed at 120 frames per second, and the resolution was fixed at 1920 $\times$ 1080 pixels. The mode of “narrow view” was applied to avoid barrel distortion (fish-eye effect). The field of view was around 0.96 m $\times$ 0.55 m. The spatial resolution of the images obtained by the camera was approximately 0.5 mm (20 pixels per centimeter). The effects of the image perspective were corrected using OpenCV, an open-source computer vision library. Previous study [30] used a particle velocimeter (PIV) to obtain particle velocity from images; the small particles used in the present study (the smallest diameter is smaller than the spatial resolution of the images) prevent from using PIV.

B. Multiphase model of Lee [24]

1. Governing equations

Based on an Eulerian-Eulerian framework, the fluid and sediment phases have their own mass and momentum balance equations. These are expressed as follows:

$$\frac{\partial \rho_f(1-c)}{\partial t} + \nabla \cdot [\rho_f(1-c)\mathbf{u}^f] = 0, \tag{1}$$

$$\frac{\partial \rho_f(1-c)\mathbf{u}^f}{\partial t} + \nabla \cdot [\rho_f(1-c)\mathbf{u}^f\mathbf{u}^f] = -(1-c)\nabla p_f + \nabla \cdot [(1-c)\mathbf{T}^f] - c\rho_s\frac{\mathbf{u}^f - \mathbf{u}^s}{\tau_p}, \tag{2}$$

for the fluid phase and

$$\frac{\partial \rho_s c}{\partial t} + \nabla \cdot (\rho_s c \mathbf{u}^s) = 0, \tag{3}$$

$$\frac{\partial \rho_s c \mathbf{u}^s}{\partial t} + \nabla \cdot (\rho_s c \mathbf{u}^s \mathbf{u}^s) = (\rho_s - \rho_f) c \mathbf{g} - c \nabla p_f - \nabla (c p_s) + \nabla \cdot (c \mathbf{T}^s) + c \rho_s \frac{(\mathbf{u}^f - \mathbf{u}^s)}{\tau_p}, \tag{4}$$

for the solid phase. In these equations, f/s in the superscripts and subscripts refer to the fluid/solid phase, ρ is the mass density, $\mathbf{u}$ is the mean velocity, $\mathbf{g}$ is the acceleration due to gravity, p is the pressure, $\mathbf{T}$ is the stress, and τ_p is the particle response time used to parametrize the interphase drag force. Note that the gravity term does not appear in Eq. (2), because p_f is the hydrodynamic pressure. A Newtonian fluid model was adopted to compute $\mathbf{T}^f$. The approach proposed by Lee and Huang [20] to compute τ_p is adopted herein and is summarized in Sec. II B 2. The closures for p_s and $\mathbf{T}^s$ are the two most important closures in the multiphase model for simulating subaqueous landslides, which are related to shear-induced volume change and the rheology of sediment. Sections II B 3 and II B 4 elaborate on how to determine p_s and $\mathbf{T}^s$ in the model proposed by Lee [24], respectively.

2. Particle response time

To compute τ_p, Lee and Huang [20] combined the approach of Richardson and Zaki [31] for falling particles and the approach of Engelund [32] for flow through porous media. The former approach is suitable for low-concentration flows and the latter approach is suitable for high-concentration flows. The resultant formula for computing the particle response time is given by [20]

$$\tau_p = \begin{cases} \frac{\rho_s}{\rho_f} \frac{d^2}{\nu_f} \frac{(1-c)^{n-3}[\max(1-c/c_o, 0)]^{c_o}}{18 + (4.5/(1+\sqrt{\mathrm{Re}_p}) + 0.3)\mathrm{Re}_p}, & \text{for } c < c_r, \\ \frac{\rho_s d^2}{\rho_f \nu_f} \frac{1}{a_E c^2 + b_E \mathrm{Re}_p}, & \text{for } c \geqslant c_r, \end{cases} \tag{5}$$

where ν_f is the kinematic viscosity; $\mathrm{Re}_p = |\mathbf{u}^s - \mathbf{u}^f| d/\nu_f$; c_r is the concentration at the intercept point of the above two equations, a_E and b_E are the model parameters for flow through porous media, and n is a parameter that captures the hindered effect [33]. For sands, $a_E = 1500$ and $b_E = 1.8$ were used [32]. $n = 0$ is considered in this study, meaning that the hindered effect is ignored. The hindered effect results from the interaction between particles and eddies caused by surrounding particles, which changes the settling velocity. In the approach of Richardson and Zaki [31], the formula for n was obtained by experiments with initially uniformly distributed particles settling in a tube filled with a fluid. When the particles are not uniformly distributed and the flow structures become more complex, the formula of Richardson and Zaki [31] for n needs further improvement. We attempted to use $n > 0$ based on the formula of Richardson and Zaki [31]. Using $n > 0$ causes slower initiation of the collapse and slower falling velocity. The slower initiation leads to the shorter runout distance but the slower falling velocity yields the longer runout distance. Our numerical results using $n > 0$ lead to a too long runout distance.

3. Solid pressure

To consider the dynamic effect from interparticle collision and the static effect from interparticle enduring contact, p_s is divided into two components:

$$p_s = p_{sd} + p_{ss}, \tag{6}$$

where p_{sd} accounts for the dynamic effect, and p_{ss} is the static effect. According to the discrete-element method (DEM) simulations [34], p_{sd} can be further divided into two components: p_{sei} because of the inertial-elastic effect, and p_{si}, resulting from inertial effects. The blending approach suggested by Chialvo *et al.* [34] is used to compute p_{sd}:

$$p_{sd} = \begin{cases} p_{sei}, & c \geqslant c_j \\ \frac{1}{1/p_{si}+1/p_{sei}}, & c < c_j \end{cases}. \tag{7}$$

p_{sei} is determined using [34]

$$p_{sei} = a_{ei}\rho_s^{1/4}E^{3/4}d^{1/4}D^{s1/2}, \tag{8}$$

with $D^s = (D^s_{ij}D^s_{ij}/2)^{1/2}$, E representing Young's modulus, and a_{ei} is a model parameter. $E = 10^6$ Pa, and $a_{ei} = 0.15$ were taken [24]. p_{si} is determined by [19]

$$p_{si} = \frac{2b_i^2 c}{(c_j - c)^2}(\rho_f \nu_f + 2a_i\rho_s d^2 D^s)D^s, \tag{9}$$

where $a_i = 0.11$, $b_i = 1$, and c_j is the concentration at the jamming point. c_j was not measured in this experiment. Few studies report c_j for sand, but many studies report c_c. c_c approaches c_j when p_{ss} is small [24]. In this study, $c_j = 0.545$ was adopted.

Lee [24] suggests the evolution equation to determine p_{ss}:

$$\frac{\partial p_{ss}}{\partial t} + \mathbf{u}^s \cdot \nabla p_{ss} = 2d_{p1}c\sqrt{|II_{D^s}|}(p_{ssc} - p_{ss}) - d_{p2}c\nabla \cdot \mathbf{u}^s - d_{p3}p_{ss}, \tag{10}$$

where $II^s_D = (D^2_{ii} - D_{ij}D_{ij})/2$ is the second main invariant of $\mathbf{D}^s$ and $p_{ssc} = p_{ss}$ in the critical state with the current concentration. d_{p1}, d_{p2}, and d_{p3} are the model parameters. $d_{p1}(c - c_c) = \tan\psi$, where ψ is the dilatation angle. Lee [24] used $d_{p1} = 4$ for glass bead. Here, $d_{p1} = 4.5$ was adopted. $d_{p2} = a_e E(c - c_o)/(c_j - c_o)$ and $d_{p3} = 100s^{-1}$ were taken as in the previous study [24].

According to the simulated results of a simple shear flow [35], p_{ssc} is given by

$$p_{ssc} = a_e E(c - c_j), \tag{11}$$

where $a_e \approx 0.1$. The first term on the right-hand side of Eq. (10) describes the relaxation of p_{ss} owing to shear. In the critical state, p_{ss} approaches p_{ssc}. The second term on the right-hand side of Eq. (10) includes the change in p_{ss} owing to compression. The third term on the right-hand side of Eq. (10) describes the rapid decline in p_{ss} to zero.

It should be noted that the blending approach in Eq. (7) avoids a singularity of p_{si} at $c = c_j$ [see Eq. (9)]. Equation (10) is the key to allowing the multiphase model to correctly produce the shear-induced volume change [24].

4. *Solid stress*

The shear-stress tensor for the sediment phase is computed by

$$\mathbf{T}^s = -\left(\tfrac{2}{3}\rho_s\nu_s\nabla \cdot \mathbf{u}^s\right)\mathbf{I} + 2\rho_s\nu_s\mathbf{D}^s, \tag{12}$$

where ν_s is the viscosity of the solid phase. To consider the friction and dilatancy effects, ν_s is given by

$$\nu_s = \frac{p_{sd}\eta_d + p_{ss}\eta_s}{2\rho_s D^s}[1 - \exp(-2D^s/m)], \tag{13}$$

where m is a constant with a small value ($m = 10^{-5}$ s^{-1}), and $\eta_{d/s}$ represents the dynamic/static friction coefficient. The formula of Trulsson *et al.* [36] is adopted to determine η_d:

$$\eta_d = \eta_1 + \frac{\eta_2 - \eta_1}{1 + I_o/I^{1/2}}, \tag{14}$$

where $I_o = 0.1$, $\eta_1 = \tan\theta_r$, with angle of repose θ_r, η_2 is the maximum friction coefficient, and I is a dimensionless parameter, with $\eta_2 = 0.85$. The dimensionless parameter I is a combination of the viscous number I_v and inertial number I_i: $I = I_v + a_i I_i^2$. The viscous number is the ratio of the viscous stress to the quasistatic shear stress associated with the weight (owing to enduring contact) and is defined by $I_v = 2\rho_f \nu_f D^s / cp_s$. The inertial number, defined by $I_i = 2dD^s/\sqrt{cp_s/\rho_s}$, is the ratio of the inertial stress to the quasistatic stress. Lee [24] applies the following formula to determine η_s:

$$\eta_s = \eta_1 + (c - c_c)d_{p1}, \tag{15}$$

where c_c is determined by

$$c_c = p_{ss}/a_e E + c_j, \tag{16}$$

without considering the dynamic effects of critical concentration. Equation (16) suggests the critical concentration increasing with the solid pressure; the tendency has been observed in previous studies [37].

Note that Eq. (13) considers the yield stress $(p_{sd}\eta_d + p_{ss}\eta_s)$ using the regularization scheme of Papanastasiou [38]. This scheme treats the nonyielded granular material as a highly viscous fluid to avoid the discontinuity problem near the yield point $|\mathbf{T}^s| = p_{sd}\eta_d + p_{ss}\eta_s$. The effect of the dilatancy angle on the friction coefficient is accounted for by the second term on the right-hand side of Eq. (15). When c is larger or smaller than c_c, the dilatancy angle is positive or negative, thus increasing or decreasing the friction coefficient.

5. *Numerical setup*

The computational domain was similar to the geometry in the experiment (see Fig. 1). In contrast, the computational domain had a 0.5-m flat bed, which was shorter than the 1.5-m flat bed in the experiment. However, all other dimensions remained the same. Regarding the boundary conditions, a no-slip boundary condition was imposed at all rigid boundaries for both phases (including the right boundary). The zero-gradient condition was used for the velocities for both phases at the top boundary. The gate in Fig. 1 was not simulated. The initial concentration was given by uniform c_i in the reservoir with $H_i = 0.1$ m and $L_i = 0.1$ m. The initial concentration outside the reservoir was zero. Initially, p_{ss} had a hydrostatic distribution in the reservoir. A total of 41 175 computational cells were used in the simulations. The cells on the inclined plane were triangular, and the other cells were rectangular and 2 mm in height. The aspect ratios of the cells increased from 1 (near the inclined plane) to 3 (far from the inclined plane); 400 cells were used adjacent to the top boundary (in the x_1 direction). A time step $\Delta t < 10^{-4}$ s was used in the simulations. Our simulation typically took two days for a physical time of 10 s using a thread on a workstation with two central processing units (Intel Xeon(R) CPU E5- 2660 v2).

C. Test conditions

Table I lists the numerical and experimental conditions. Four particle sizes were used. The properties of particle have been mentioned in Sec. II A. In the simulations, $c_i = 0.55$, 0.56, 0.57, and 0.6 were used. The experiments used only $c_i = 0.6$. Both the height and the width of the granular mass in the reservoir were 0.1 m. The model parameters are summarized in Table II.

III. RESULTS AND DISCUSSIONS

A. Collapse processes

The model of Lee [24] was validated by the experiments of Rondon *et al.* [8], in which the granular columns consisting of glass beads ($d = 0.225$ mm) collapsed on a horizontal plane within a highly viscous fluid ($\nu_f = 1.2 \times 10^{-5}$ m^{2}s^{-1}). In this study, the model of Lee [24] was further validated by conducting experiments in which four types of particles and water ($\nu_f = 1 \times 10^{-6}$ m^{2}s^{-1}) was used.

TABLE I. Test conditions.

Case	d (mm)	c_i	Simulation	Experiment
F55	0.2	0.55	Yes	No
F56	0.2	0.56	Yes	No
F57	0.2	0.57	Yes	No
F60	0.2	0.60	Yes	Yes
M55	0.49	0.55	Yes	No
M56	0.49	0.56	Yes	No
M57	0.49	0.57	Yes	No
M60	0.49	0.60	Yes	Yes
C55	0.66	0.55	Yes	No
C56	0.66	0.56	Yes	No
C57	0.66	0.57	Yes	No
C60	0.66	0.60	Yes	Yes
VC55	1.29	0.55	Yes	No
VC56	1.29	0.56	Yes	No
VC57	1.29	0.56	Yes	No
VC60	1.29	0.55	Yes	Yes

The simulated collapse processes are compared with the measured ones in Fig. 2, including the four different particle sizes, that is, fine sand, medium sand, coarse sand, and very coarse sand. For the experiments, the granular materials had darker areas in the video-recorded images. For the simulated results, the colored lines were considered as contour lines and were used to indicate the simulated water-sand surfaces. Because the concentration cannot be identified in the images, the simulated contour lines of $c = 10^{-3}$, 0.09, and 0.4 are plotted in the figure. The values of 0.09, and 0.4 are suggested as thresholds to identify different sedimentary flow types: turbidity currents ($c \leqslant 0.09$), concentrated flow ($0.09 < c \leqslant 0.4$), and hyperconcentrated flow ($c > 0.4$) [39]. The value of $c = 10^{-3}$ is used to distinguish clear water from turbid water [40].

Referring to Fig. 2, the measured results show that the fine sand (Case F60) has a breaching process, where the particles are spalled near the vertical face and the front of the column retreats slowly. As the particle size increases, the sliding process transforms from the breaching process to the slumping process, where the sliding material deforms and the upper right parts slide down. There is a vortex behind the sliding front, which suspends the particles and can be identified by the gray cloud in each case. Note that for Case F60 most particles have been deposited at $t = 12$ s, but there are still a few particles suspended.

Although the simulated results generally agree with the measured results for the four cases shown in Fig. 2, a discrepancy can be observed in the deposition for Case F60, where the simulated result has a deposition slightly farther than the measured one. The formula used to determine the

TABLE II. Model parameters.

Parameter	Value	Parameter	Value	Parameter	Value
a_e	0.1	a_E	1500	a_{ei}	0.15
a_i	0.11	b_E	1.8	b_i	1
c_o	0.54	c_j	0.545	d_{p1}	4.5
d_{p2}	100 s^{-1}	E	10^6 Pa	I_o	0.1
m	10^{-5} s^{-1}	n	0	η_1	0.7
η_2	0.85				

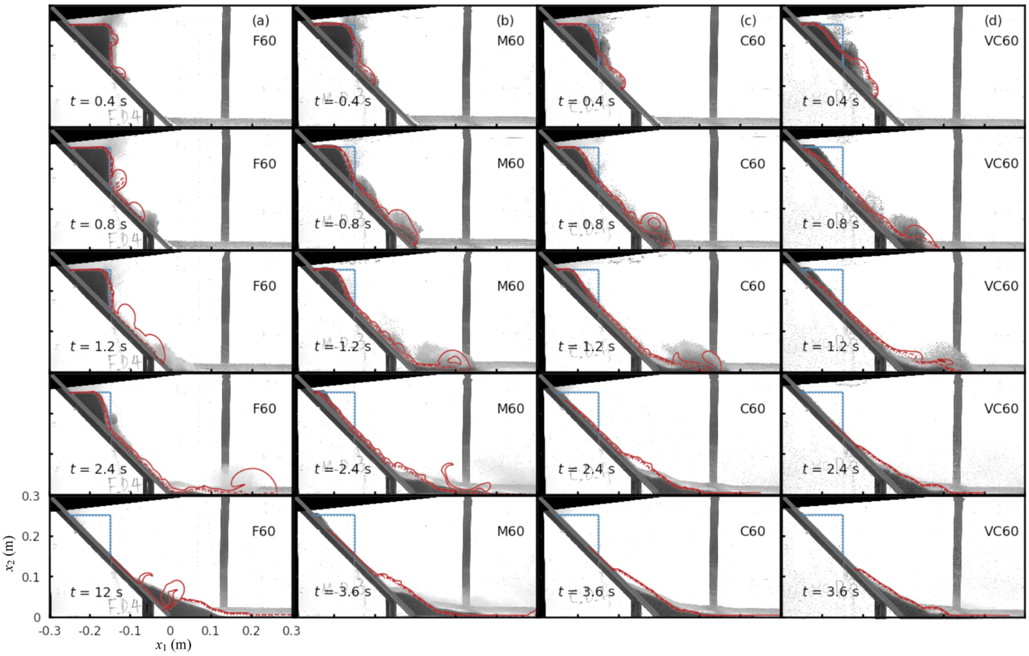

FIG. 2. Snapshots of the observed and simulated landslide processes for (a) Case F60, (b) Case M60, (c) Case C60, and (d) Case VC60. The simulated contour lines of $c = 10^{-3}$ (solid red lines), $c = 0.09$ (dashed red lines), and $c = 0.4$ (dotted red lines) are included for comparison with the observed fluid-sand interface. The blue line in each plot outlines the initial shape of the granular material on the slope. Animations can be found online [44].

particle response time, Eq. (5) might be responsible for the discrepancy, which affects the drag force $[c\rho_s(\mathbf{u}^f - \mathbf{u}^s)/\tau_p$, the last terms in Eqs. (2) and (4)] and the falling velocity. In this study, $n = 0$ in Eq. (5) is adopted, neglecting the effect of the surrounding particles on τ_p and on the drag force. Previous studies [41] suggest that the appearance of surrounding particles can increase or decrease the drag force, depending on the arrangement. If the drag force is reduced, the deposition process can occur rapidly, resulting in a shorter runout distance. At present, most models adopt $n > 0$, as suggested by Richardson and Zaki [31], which increases the drag force. Our numerical experiments revealed a longer runout distance when using $n > 0$. Consequently, Eq. (5) needs improvement by better considering effects of particle arrangements on τ_p.

It is noticed that the overestimation of runout distance occurs only for Case F60 but not for Cases M60, C60, and VC60. Case F60 has a longer collapse duration (around 12 s) than Cases M60, C60, and VC60 (around 3.6 s). The longer duration may magnify the drawback of Eq. (5); this may be the reason why the overestimation exists only for Case F60.

Figure 3 displays the simulated front location (x_{front} in the x_1 direction) and the measured ones before touching the flat bed for Cases F60, M60, C60, and VC60. The simulated sliding fronts defined using $c = 10^{-3}$ and $c = 0.09$ are similar. The simulated front locations agree with the measured ones generally. It can be observed from Fig. 3 that the sliding fronts have an acceleration phase (e.g., $t < 0.3$ s for Case M60), followed by a nearly constant-speed phase (e.g., $t > 0.3$ s for Case M60). The front speed will be further examined in Sec. III D.

B. Flow fields

This section numerically examines the flow fields in the early stages and in the development stage of the collapse process. Figure 4 compares the simulated flow fields of the solid phase at

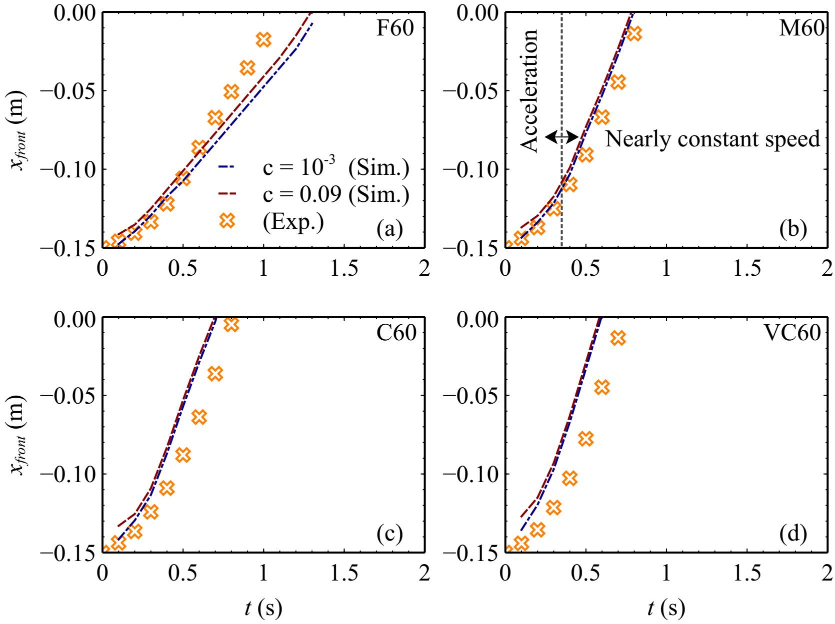

FIG. 3. Simulated and measured time series of front position for (a) Case F60, (b) Case M60, (c) Case C60, and (d) Case VC60.

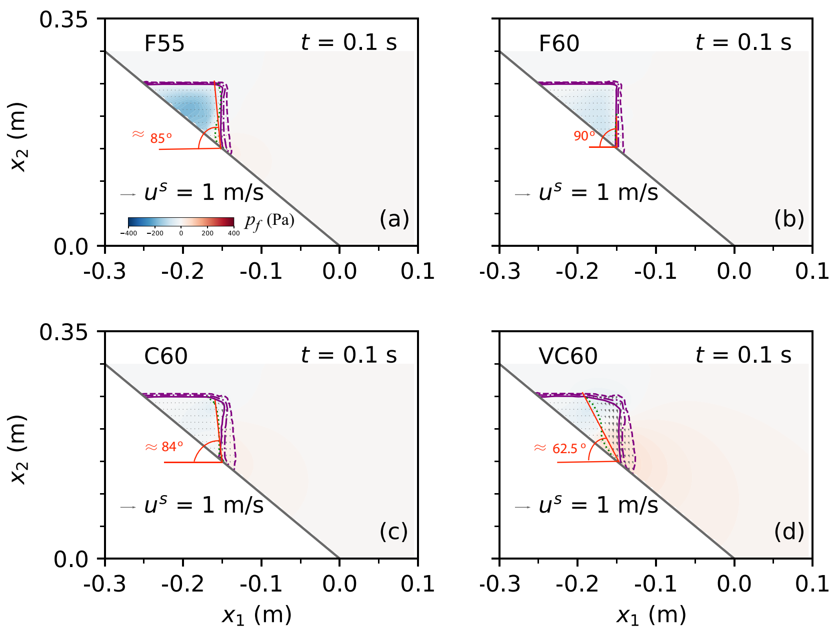

FIG. 4. Velocity fields of the solid phase and the pressure fields of the fluid phase for (a) Case F55, (b) Case F60, (c) Case C60, and (d) Case VC60. The color maps present the fluid pressure, and the arrows show the solid velocity. The dashed lines are the contour lines of $c = 10^{-3}$, the dashed-dotted lines are $c = 0.09$, the solid lines are $c = 0.4$, and the dotted lines are the contour lines of $|\mathbf{u}^s|$=0.05 m/s.

$t = 0.1$ s (the early stage) for four cases: cases F55, F60, C60, and VC60. The contour lines of $|\mathbf{u}^s| = 0.05$ m/s are included in Fig. 4; our numerical experiments suggest that the contour lines of $|\mathbf{u}^s| = 0.05$ m/s can separate the flow and static regions. The contour lines of $|\mathbf{u}^s| = 0.05$ m/s are considered failure lines [42] A trial and error method was used to define the failure line by the contour line of $|\mathbf{u}^s| = 0.05$ m/s, which can separate the flow and static regions. Additionally, the contour lines of $|\mathbf{u}^s| = 0.05 \pm 0.02$ m/s are nearly identical Cases F60 and C60 have straight failure lines, and the s-shaped failure lines are revealed in Cases F55 and VC60. The failure lines cross the toe of the sliding masses as in the previous study of granular collapses [43]. The s-shaped failure lines were approximated by straight lines. It is noticed that the straight failure line is the simplest approximation used in the failure analysis of slope and is suitable for near vertical slopes [13]. The angle between the failure line and the horizontal line is considered as the failure angle θ_f. Case F60 has $\theta_f \approx 90^o$, meaning that the sediment particle spalled from the vertical surface, which is consistent with the breaching process. Case VC60 has $\theta_f \approx 62.5^o$, which is equal to $45^o + \theta_r/2$ suggested by Rankine to determine the failure angle of a subaerial slope [13]. Comparing the four cases, θ_f increases with increasing c_i and decreasing d.

A negative pore pressure exists inside the sediment material for the four cases, which results from the shear dilation and can stabilize the initial granular material [8,24]. Here, c_c is approximated by c_j according to Eq. (16) with low p_{ss}. Because c_i exceeds $c_c \approx 0.545$, the shear decreases c and enlarges the interstitial space between the particles. Then, negative pore pressure impacts the absorption of water into the sediment material. The magnitude of the negative pore pressure depends on $1/\tau_p$ (measuring the difficulty in absorbing water) and dilation rate ($\tan\psi\,\partial u_s^s/\partial x_n$, where u_s^s is the velocity along the failure line and x_n is the axis normal the failure line) [14]. However, it is not easy to determine how c_i affects the pore pressure because growing c_i increases $\tan\psi$ but decreases $\partial u_s^s/\partial x_n$ through the friction [Eq. (15)].

Figure 5 presents the flow structures of sedimentary flow in the developed stages for Cases F55, F60, and VC60. The instants for the three cases in Fig. 5 are $t = 0.75$, 1.3, and 0.61 s when the sliding fronts touch the flat bottom. Here, the sedimentary flow is classified into the turbidity region ($10^{-3} \leqslant c \leqslant 0.09$), the concentrated region ($0.09 < c \leqslant 0.4$), and the hyperconcentrated region ($c > 0.4$). The three regions have different flow properties. The flow in the hyperconcentrated region is a non-Newtonian flow, and the flow in the other two regions are Newtonian flow [39]. The vortices due to Kelvin-Helmholtz instability stir the turbidity region and suspend sediment particles [45]. As shown in Fig. 5, the solid pressure vanishes in the concentrated and turbidity regions, meaning that the solid stress is free [Eq. (13)] and that flow is Newtonian. Additionally, vortices stirring the turbidity region can be observed in Fig. 5.

Figure 5(a) shows that sedimentary flow ($|\mathbf{u}^s| > 0$ m/s) in Case F55 has all three regions coexisting (the turbidity region, the concentrated region, and the hyperconcentrated region). In Case F60, fewer particles are released and the fine sand is easily suspended, resulting in the domination of the turbidity region [Fig. 5(c)]. In Case VC60, the hyperconcentrated flow dominates, as shown in Fig. 5(e). When compared to Case F60, Case VC60 has coarser particles, which is more difficult to suspend. It can be concluded that the sedimentary flow due to sliding has different flow structures (three flow region coexistence, turbidity region domination, and hyperconcentrated flow domination), depending on the initial concentration and the particle size.

C. Sliding mass in the early collapse stage

The particle size and initial concentration affect the collapse type, causing different volumes of the initial sliding mass. The volume of the initial sliding mass is hereinafter referred to as the initial sliding volume.

The initial sliding volume is determined using the solid volume with the solid velocity $|\mathbf{u}^s| > 0.05$ m/s, which can effectively distinguish the sliding layer and static layer, as shown in Fig. 4. When a collapse begins, the sliding layer accelerates from a static state. The sediment velocity at $t = 0.1$ s was adopted to quantify the initial sliding volume.

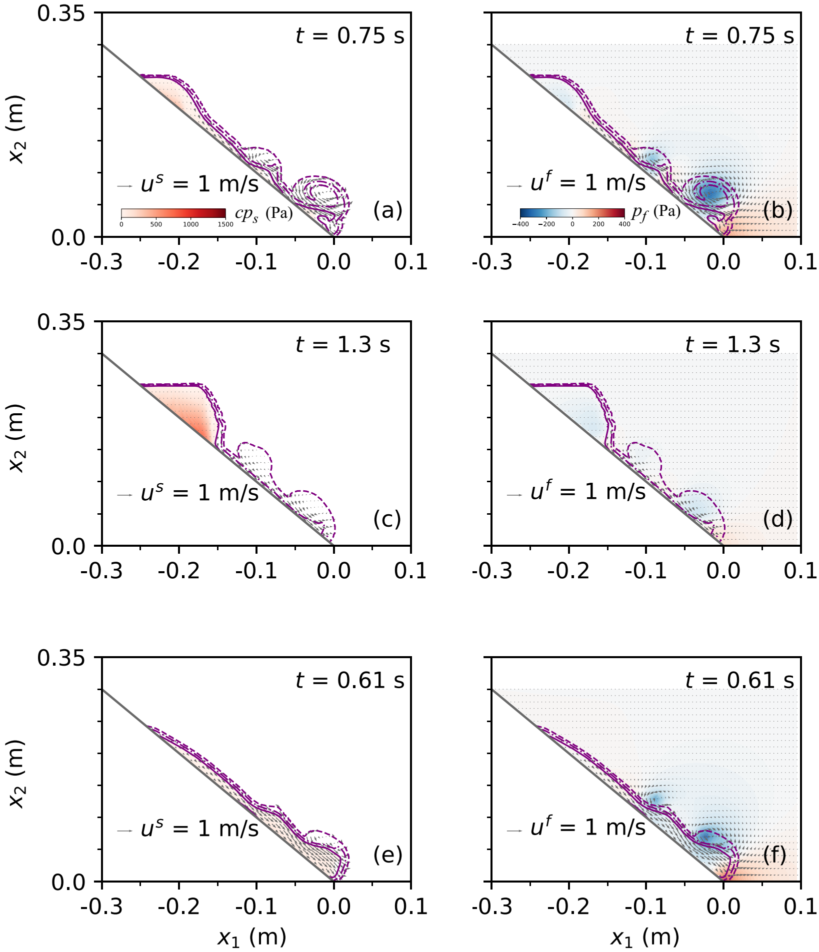

FIG. 5. Flow fields of the solid and fluid phases for (a) and (b) Case F55, (c) and (d) Case F60, and (e) and (f) Case VC60. The color maps represent the solid pressure (a), (c), and (e) and the water pressure (b), (d), and (f). The arrows show the solid velocity (a), (c), and (e) and water velocity (b), (d), and (f). The dashed lines are the contour lines of $c = 10^{-3}$, the dashed-dotted lines are $c = 0.09$, the solid lines are $c = 0.4$, and the dotted lines are the contour lines of $|\mathbf{u}^s|$=0.05 m/s.

Figure 6 depicts the initial sliding volume ($\int_\Omega c\ |_{u^s>0.05}\ dv$ with Ω being the whole computational domain and dv being the volume element) normalized by the total volume ($\int_\Omega c dv$), m^*, against the particle size and initial concentration. As shown in Fig. 6(i) larger d yields more m^*, (ii) increasing c_i reduces m^*, (iii) m^* approaches 0.52 for very coarse sand ($d = 1.29$ mm) with any initial concentration.

The initial sliding volume is associated with the failure line. A straight failure line passing through the toe of the sliding material is considered in the Culmann method to determine the slope stability [13]; the sediment above the straight failure is accounted for in the initial sliding volume. $m^* \approx 0.52$ corresponds to $\theta_f = 62.5^o$ $(= 45^o + \theta_r/2)$, which is identical to θ_f for dry granular material. For the breaching case (e.g., Case F60), θ_f is close to 90°. In Fig. 6, the fine sand ($d = 0.2$ mm) with $c_i > 0.56$ results in $m^* < 0.017$ (corresponding to $\theta_f > 89^o$), suggesting a breaching slide process.

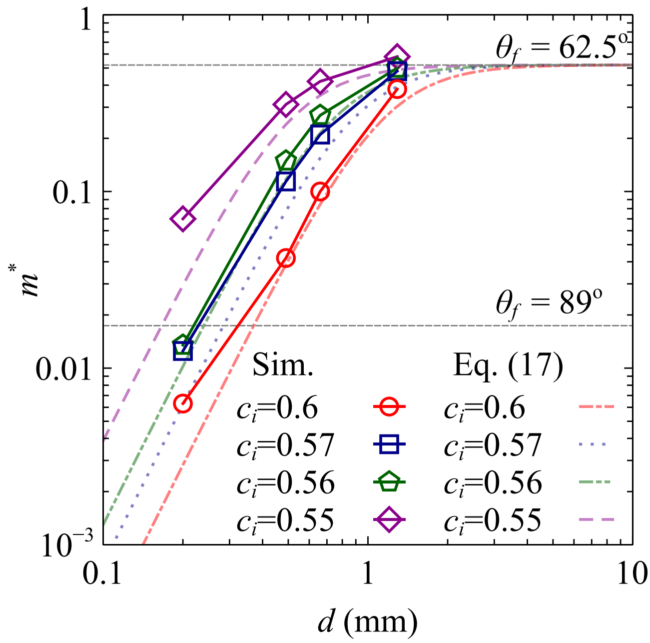

FIG. 6. Dimensionless volume of the sliding mass at $t = 0.1$ s.

According to the above discussion, the relationship between the initial sliding volume and particle size can be expressed by the formula:

$$m^* = \cot\left[45^o + \frac{\theta_r}{2} + \frac{45^o - \theta_r/2}{1 + 0.001 d^{*3}/(c - c_c)}\right], \tag{17}$$

where $d^* = [\rho_s(\rho_s/\rho_f - 1)g/\rho_f^2 \nu_f^2]^{1/3} d$. d^* is proportional to $St^{1/3}$. The value of 0.001 in Eq. (17) was obtained with the minimum mean squared logarithmic error of 0.008 in the nonlinear regression analysis. Equation (17) is also included in Fig. 6.

This section presents the significant effects of d and c_i on m^*. Those effects might result from the dilation behavior and the pore-pressure feedback, which will be further examined by using a simplified model based on a force analysis in Sec. IV.

D. Sliding front speed

Figure 7 presents the simulated sliding front speed ($u_{\text{front}//}$ along the slope) for different particle sizes and different initial concentrations. The measured ones are also included in Fig. 7 for comparison. The sliding front speed was determined by the mean rate of change of x_{front} within -0.1 m $< x_{\text{front}} < 0$ m. Both the simulated and the measured results reveal that the front speed increases and approaches $u_{\text{front}//} \approx 0.46$ m/s with increasing d. The simulated results show the front speed increases with reducing c_i. The sliding front speeds largely exceed the falling velocity of particles in quiescent water (0.03 m/s for $d = 0.2$ mm and 0.15 m/s for $d = 1.29$ mm). The order of the magnitude of the sliding front speed is the same as $O(\sqrt{g' H_i})$ with $g' = (\rho_s - \rho_f)g/\rho_s$. It should be noted that $\sqrt{g' H_i} = 0.78$ m/s.

Some previous studies analyzed the flow-front speed of the density flow (flow of a heavy fluid with a light ambient fluid) [46]. The flow-front speed of the density flow depends on the initial weight of the density flow. The dimensionless sliding front speed ($u^*_{\text{front}//} = u_{\text{front}//}/(g' H_i)^{0.5}$) against the dimensionless initial sliding volume (proportional to the initial weight) is shown in

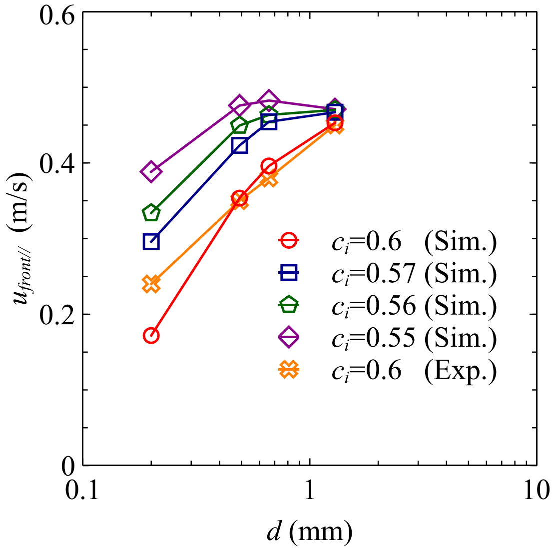

FIG. 7. Front speed versus the particle size and the initial concentration.

Fig. 8. The following relationship between $u^*_{\mathrm{front}//}$ and m^* is revealed in Fig. 8:

$$u^*_{\mathrm{front}//} = \frac{0.6}{1 + 0.009/m^*}. \tag{18}$$

The values of 0.6 and 0.009 in Eq. (18) were obtained with the minimum mean squared error of 0.0008 in the nonlinear regression analysis.

The initial sliding mass ran ahead of the mass released later and contributed to the formation of the sliding front. The gravitational force applied on the sliding front (formed by the initial sliding mass) is balanced by the drag force and the bed friction force, both depending on velocity. It seems

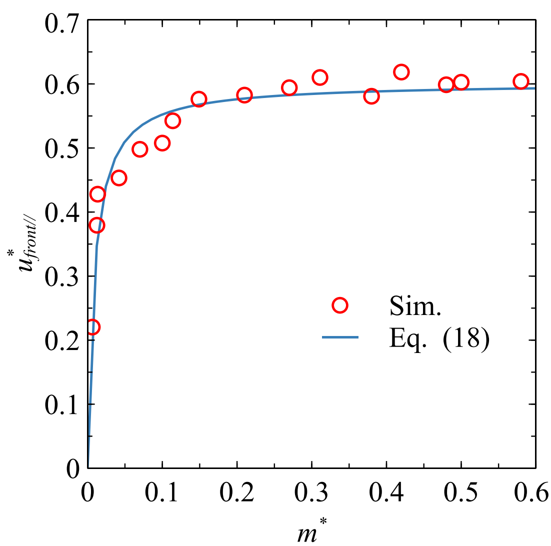

FIG. 8. The sliding front speed against the initial sliding volume.

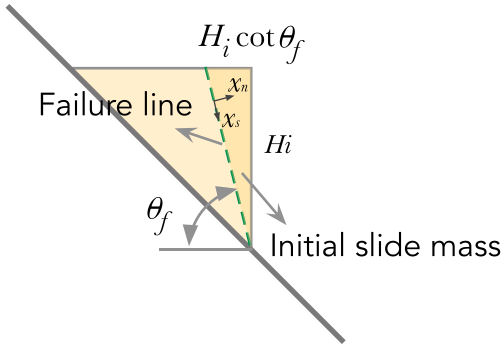

FIG. 9. Schematic of the initial sliding mass.

reasonable that there exists the relationship between the sliding front speed and the initial sliding volume. This relationship explains why Figs. 6 (m^* vs d and c_i) and 7 ($u_{\mathrm{front}//}$ vs d and c_i) have similar patterns.

IV. SIMPLIFIED MODEL FOR THE INITIAL SLIDING MASS

Force analysis was performed to determine the initial sliding mass. Following the Culmann method [13], the failure line is assumed to be a straight line passing through the toe of the total granular mass, as shown in Fig. 9. Along the failure line, the average shear stress of the solid phase τ exceeds the shear strength of the sediment, which can be expressed by $\sigma \tan\theta_r$, where σ is the average normal stress according to the Coulomb failure criterion. Additionally, $\tau - \sigma \tan\theta_r$ has its maximum on the failure line; in other words, the failure line has

$$\frac{\partial(\tau - \sigma \tan\theta_r)}{\partial\theta_f} = 0. \tag{19}$$

In contrast to the Culmann method for determining the failure line of the subaerial slope, the dilation induced pore pressure should be considered in this study.

In the early collapse process, the sliding mass is in a quasistatic state, and the inertia of the sliding mass and the inertia of the pore fluid can be ignored. To simplify this problem, (i) the viscous stress of the fluid is neglected; (ii) the fluid and sediment have the same velocity in the x_n direction, but not in the x_s direction; (iii) the shear rate is uniform; and (iv) c_i is uniform.

The average shear stress on the failure line can be determined through the weight of the initial sliding mass in the x_s direction as follows:

$$\tau = \tfrac{1}{4}c_i\rho_s g' H_i \sin 2\theta_f, \tag{20}$$

where $g' = (\rho_s - \rho_f)g/\rho_s$. In addition to the weight, the buoyancy and drag force must be considered in the averaged normal stress:

$$\sigma = \frac{1}{2}c_i\rho_s g' H_i \cos^2\theta_f + \frac{\sin\theta_f}{H_i}\iint\left[c_i\frac{\partial p_f}{\partial x_n} - \frac{c_i\rho_s\left(u_n^f - u_n^s\right)}{\tau_p}\right]dx_n dx_s. \tag{21}$$

Owing to the momentum balance of the fluid in the x_n direction, Eq. (2) yields

$$c_i\rho_s\frac{\left(u_n^f - u_n^s\right)}{\tau_p} = -(1-c_i)\frac{\partial p_f}{\partial x_n}. \tag{22}$$

When dilation occurs, the interstice between particles increases, and the increment of the interstice must be filled with fluid. In this problem, only dilation causes u_n^f and u_n^s. According to the

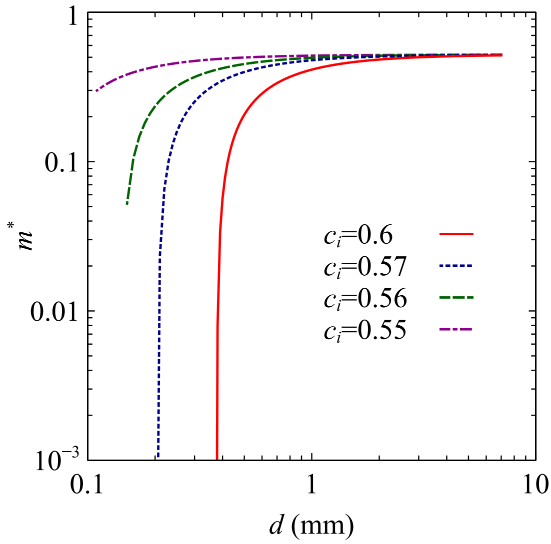

FIG. 10. m^* predicted by the simplified model for different c_i and d.

conservation of mass, u_n^f and u_n^s have the following relationship:

$$(1 - c_i)u_n^f = -c_i u_n^s. \tag{23}$$

For shear-induced dilation problems, $\partial u_n^s/\partial x_n = \tan\Psi \partial u_s^s/\partial x_n$ [17]. A uniform shear rate was assumed. $\tan\Psi$ can be approximated by $d_{p1}(c - c_c)$ [24], where c_c is close to c_j in this study. Consequently, $\partial u_n^s/\partial x_n = \tan\Psi \partial u_s^s/\partial x_n$ becomes

$$u_n^s = u_s^s d_{p1}(c_i - c_j). \tag{24}$$

Substituting Eqs. (5), (22), and (23) into Eq. (21) yields

$$\sigma = \frac{1}{2}c_i\rho_s g' H_i \cos^2\theta_f + H_i\cos\theta_f \frac{a_E d_{p1} c_i^2 (c_i - c_j)\rho_f \nu_f}{(1 - c_i)d^2}\bar{u}_s^s, \tag{25}$$

where $\bar{u}_s^s$ is the mean velocity of the sliding mass. It is noted that the velocities of both phases are small, so the fluid inertia is neglected when computing τ_p.

Equations (19), (20), and (25) were solved numerically with $\bar{u}_s^s = 0.12\sqrt{g'd}$ [47]. The obtained θ_f was used to compute the initial sliding volume $c_i \cot\theta_f H_i^2/2$. It is remarked that using $\bar{u}_s^s/\sqrt{g'd} = 0.12$ yields the initial sliding volume close to the multiphase simulated result for $c_i = 0.57$ and $d = 0.2$ mm. Increasing $\bar{u}_s^s$ reduces the initial sliding volume. The dismalness initial sliding volume $m^* = \cot\theta_f$ is shown in Fig. 10, which has similar patterns with Fig. 6 in quality. The value of m^* increases with increasing d and decreasing c_i. In the simplified model, the effect of d and c_i are raised from the second term in Eq. (25) which accounts for the shear-induced volume change and pore pressure feedback. It can be concluded that d and c_i affect m^* mainly through the shear-induced volume change and pore pressure feedback.

It is noticed that the inclined plane with the angle of 45° plays no role in the force analysis. The reason is that the failure angle (>62.5^o) is larger than the slope angle 45°. The inclined plane does not affect the failure angle. If the slope angle exceeds 62.5^o, the effect of the slope angle on the failure angle should be considered.

V. CONCLUSIONS

Multiphase simulations and experiments of subaqueous granular collapse on an inclined plane under densely packed conditions were performed in this study. The experimental results of the collapse process for four particle sizes (fine sand, medium sand, coarse sand, and very coarse sand) agree with the simulated results using the multiphase model of Lee [24], generally. The formula to compute the particle response time needs improvement, which might be responsible for overestimating the runout distance for fine sand. Based on the simulated results, the following conclusions were drawn.

The initial sliding volume increases with the particle size but decreases for the higher initial concentration, which can be expressed by

$$m^* = \cot\left[45^o + \frac{\theta_r}{2} + \frac{45^o - \theta_r/2}{1 + 0.001 d^{*3}/(c - c_c)}\right].$$

Decreasing the initial concentration and increasing the particle size enlarges the sliding front speed.

The front speed is the function of the initial sliding volume:

$$u^*_{\text{front}//} = \frac{0.6}{1 + 0.009/m^*}.$$

The initial concentration and the particle size affect the sedimentary flow structures.

The simplified force analysis suggested that the particle size and initial concentration affect the initial sliding mass through shear dilation and pore-pressure feedback.

ACKNOWLEDGMENTS

The material is based on work supported by the Ministry of Science and Technology, Taiwan [MOST 110-2636-E-110-010]. The authors report no conflict of interest.

[1] M. A. Hampton, H. J. Lee, and J. Locat, Submarine landslides, Rev. Geophys. **34**, 33 (1996).

[2] J. Kim, F. Løvholt, D. Issler, and C. F. Forsberg, Landslide material control on tsunami genesis—the Storegga slide and tsunami (8,100 Years BP), J. Geophys. Res. **124**, 3607 (2019).

[3] C. Zhu, S. Cheng, Q. Li, H. Shan, J. Lu, Z. Shen, X. Liu, and Y. Jia, Giant submarine landslide in the South China Sea: Evidence, causes, and implications, J. Mar. Sci. Eng. **7**, 152 (2019).

[4] I. Sepúlveda, J. S. Haase, M. Carvajal, X. Xu, and P. L. F. Liu, Modeling the sources of the 2018 Palu, Indonesia, tsunami using videos from social media, J. Geophys. Res. **125**, e2019JB018675 (2020).

[5] R. Bruschi, S. Bughi, M. Spinazzé, E. Torselletti, and L. Vitali, Impact of debris flows and turbidity currents on seafloor structures, Norw. J. Geol. **86**, 317 (2006).

[6] S.-K. Hsu, J. Kuo, C.-L. Lo, C.-H. Tsai, W.-B. Doo, C.-Y. Ku, and J.-C. Sibuet, Turbidity currents, submarine landslides and the 2006 Pingtung earthquake off SW taiwan, Terr. Atmospheric Ocean. Sci. **19**, 767 (2008).

[7] C. Meruane, A. Tamburrino, and O. Roche, On the role of the ambient fluid on gravitational granular flow dynamics, J. Fluid Mech. **648**, 381 (2010).

[8] L. Rondon, O. Pouliquen, and P. Aussillous, Granular collapse in a fluid: role of the initial volume fraction, Phys. Fluids **23**, 73301 (2011).

[9] C. Wang, Y. Wang, C. Peng, and X. Meng, Dilatancy and compaction effects on the submerged granular column collapse, Phys. Fluids **29**, 103307 (2017).

[10] A. Bougouin and L. Lacaze, Granular collapse in a fluid: Different flow regimes for an initially dense-packing, Phys. Rev. Fluids **3**, 064305 (2018).

[11] C.-H. Lee, Z. Huang, and M.-L. Yu, Collapse of submerged granular columns in loose packing: Experiment and two-phase flow simulation, Phys. Fluids **30**, 123307 (2018).
[12] C.-H. Lee, Underwater collapse of a loosely packed granular column on an inclined plane : Effects of the Darcy number, AIP Adv. **9**, 095046 (2019).
[13] B. M. Das, *Principles of Geotechnical Engineering* (Cengage Learning, Stamford, 2013).
[14] M. Pailha and O. Pouliquen, A two-phase flow description of the initiation of underwater granular avalanches, J. Fluid Mech. **633**, 115 (2009).
[15] D. L. George and R. M. Iverson, A depth-averaged debris-flow model that includes the effects of evolving dilatancy. I. Physical basis, Proc. Math. Phys. Eng. Sci. **470**, 20130819 (2014).
[16] F. Bouchut, E. D. Fernández-Nieto, A. Mangeney, and G. Narbona-Reina, A two-phase two-layer model for fluidized granular flows with dilatancy effects, J. Fluid Mech. **801**, 166 (2016).
[17] S. Roux and F. Radjai, Texture-dependent rigid plastic behaviour, in *Physics of Dry Granular Media*, edited by H. J. Hermann, J. P. Hovi, and S. Luding (NATO ASI Series, Overijse, Belgium, 1997), pp. 305–311.
[18] F. Bouchut, E. D. Fernández-Nieto, E. H. Koné, A. Mangeney, and G. Narbona-Reina, A two-phase solid-fluid model for dense granular flows including dilatancy effects: Comparison with submarine granular collapse experiments, EPJ Web Conf. **140**, 09039 (2017).
[19] C.-H. Lee, Y. M. Low, and Y.-M. Chiew, Multi-dimensional rheology-based two-phase model for sediment transport and applications to sheet flow and pipeline scour, Phys. Fluids **28**, 053305 (2016).
[20] C.-H. Lee and Z. Huang, A two-phase flow model for submarine granular flows: With an application to collapse of deeply-submerged granular columns, Adv. Water Res. **115**, 286 (2018).
[21] C.-H. Lee and Z. Huang, Multi-phase flow simulation of impulsive waves generated by a sub-aerial granular landslide on an erodible slope, Landslides **18**, 881 (2021).
[22] P. Si, H. Shi, and X. Yu, Development of a mathematical model for submarine granular flows, Phys. Fluids **30**, 083302 (2018).
[23] H. Shi, P. Dong, X. Yu, and Y. Zhou, A theoretical formulation of dilatation/contraction for continuum modelling of granular flows, J. Fluid Mech. **916**, A56 (2021).
[24] C.-H. Lee, Two-phase modelling of submarine granular flows with shear-induced volume change and pore-pressure feedback, J. Fluid Mech. **907**, A31 (2021).
[25] S. T. Grilli and P. Watts, Tsunami generation by submarine mass failure. I: modeling, experimental validation, and sensitivity analyses, J. Waterway Port Coast. Ocean Eng. **131**, 283 (2005).
[26] A. Zakeri, K. Høeg, and F. Nadim, Submarine debris flow impact on pipelines – Part I: Experimental investigation, Coast. Eng. **56**, 1 (2009).
[27] In the present study, two layers of particle (very coarse sand) were randomly glued onto the surface of the bottom and the slope. The top layer had the sparse particles and the bottom layer had the dense particles. According to discrete element simulation results of Jing *et al.* [48], such bottom and slope can create the no-slip boundary condition when the size of flowing particles is larger than or equal to the size of particles glued on the bottom and the slope.
[28] G. R. Farrell, K. M. Martini, and N. Menon, Loose packings of frictional spheres, Soft Matter **6**, 2925 (2010).
[29] The concentration is the ratio of the total volume of solid particles (excluding void) to the total volume of the granular column (including void) in the reservoir.
[30] M. Pilvar, M. J. Pouraghniaei, and A. Shakibaeinia, Two-dimensional sub-aerial, submerged, and transitional granular slides, Phys. Fluids **31**, 113303 (2019).
[31] J. F. Richardson and W. N. Zaki, Sedimentation and fluidisation: Part I, Trans. Inst. Chem. Eng. **32**, S82 (1954).
[32] F. Engelund, *On the Laminar and Turbulent Flows of Ground Water Through Homogeneous Sand* (Danish Academy of Technical Sciences, Copenhagen, 1953).
[33] X. Yin and D. L. Koch, Hindered settling velocity and microstructure in suspensions of solid spheres with moderate Reynolds numbers, Phys. Fluids **19**, 093302 (2007).
[34] S. Chialvo, J. Sun, and S. Sundaresan, Bridging the rheology of granular flows in three regimes, Phys. Rev. E **85**, 021305 (2012).

[35] J. Sun and S. Sundaresan, A constitutive model with microstructure evolution for flow of rate-independent granular materials, J. Fluid Mech. **682**, 590 (2011).

[36] M. Trulsson, B. Andreotti, and P. Claudin, Transition from the Viscous to Inertial Regime in Dense Suspensions, Phys. Rev. Lett. **109**, 118305 (2012).

[37] X. Kang, Z. Xia, R. Chen, L. Ge, and X. Liu, The critical state and steady state of sand: A literature review, Mar. Georesources Geotechnol. **37**, 1105 (2019).

[38] T. C. Papanastasiou, Flows of materials with yield, J. Rheol. **31**, 385 (1987).

[39] T. Mulder and J. Alexander, The physical character of subaqueous sedimentary density flow and their deposits, Sedimentology **48**, 269 (2001).

[40] Reference [39] recommend using the value of $c = 10^{-4}$ to distinguish clear water from turbid water. However, $c = 10^{-4}$ is too dilute (only 1.6 particles per cubic centimeter for medium sand) to see from the video-recorded images.

[41] S. C. Liang, T. Hong, and L. S. Fan, Effects of particle arrangements on the drag force of a particle in the intermediate flow regime, Int. J. Multiph. Flow **22**, 285 (1996).

[42] A trial and error method was used to define the failure line by the contour line of $|\mathbf{u}^s| = 0.05$ m/s, which can separate the flow and static regions. Additionally, the contour lines of $|\mathbf{u}^s| = 0.05 \pm 0.02$ m/s are nearly identical.

[43] E. Lajeunesse, J. B. Monnier, and G. M. Homsy, Granular slumping on a horizontal surface, Phys. Fluids **17**, 103302 (2005).

[44] https://data.mendeley.com/datasets/b935tf7cpt/1.

[45] C.-H. Lee, Multi-phase flow modeling of submarine landslides: Transformation from hyperconcentrated flows into turbidity currents, Adv. Water Resour. **131**, 103383 (2019).

[46] A. Dai, Experiments on gravity currents propagating on different bottom slopes, J. Fluid Mech. **731**, 117 (2013).

[47] Here the shear-induced volume change is examined, which occurs in the early collapse stage. The particles are driven by gravity from the static state. The length scale of shear-induced volume change is d. Therefore, it is assumed $\bar{u}_s^s \propto \sqrt{g'd}$.

[48] L. Jing, C. Y. Kwok, Y. F. Leung, and Y. D. Sobral, Characterization of base roughness for granular chute flows, Phys. Rev. E **94**, 052901 (2016).